Dynamic Prediction Model for a Lifecycle Process of Multi-Layer Oil Reservoir in porous media

Jiaxin Wang[1,2*], Leng Tian[1,2], Zongke Liu[1,2], Zechuan Wang[1,2], Can Huang[1,2]

1 State Key Laboratory of Petroleum Resources and Prospecting, China University of Petroleum (Beijing), Beijing 102249, China

2 Institute of Petroleum Engineering, China University of Petroleum (Beijing), Beijing 102249, China

ABSTRACT

To obtain sustainable economical oil production and recovery of investment, commingling production has been widely used in multi-layer oil reservoirs. However, the characteristics of oil-water flow in porous media have long been neglected, making variations in multi-layer co-production (MLCP) difficult to anticipate. This paper concentrates on complex seepage and pore throat characterizations, as well as the construction of a prediction model capable of monitoring the dynamic behavior of MLCP in microscopically variable porous media. More specifically, high-pressure mercury injection (HPMI) and nuclear magnetic resonance (NMR) were used to characterize pore throat sizes and distributions, and a capillary bundle model was used to assess water displacement seepage resistance. In the process of continuous water parallel displacement, the changes in seepage resistance induced by throat altering and coupling boundary layer effects were especially explored. As a consequence, using the time-node analysis approach, a thorough mathematical model was built and confirmed by comparing experimental results. With errors of 3.94 % and 1.62 %, the projected oil recovery and water cut from the created model are in excellent agreement with actual findings.

Keywords: Multi-layer co-production, porous media, Seepage resistance, Boundary layer, Dynamic prediction mathematical model.

NONMENCLATURE

Variables	The meaning of represents	Unit
ρ	Transverse surface relaxivity rate	$\mu m/ms$
c	Shape factor (in general, shape factor is 2)	/
P_c	Capillary pressure	MPa
σ	Interfacial water-crude oil system	mN/m
ϑ	Contact angle	°
r	Throat radius	μm
h	Boundary layer thickness	μm
P_I	Additional resistance due to wetting lag	MPa
ϑ'	Advance Angle	°
ϑ''	Receding angle	°
P_{II}	Resistance of capillary effect	MPa
P_f	Fluid viscous resistance in throat with length L	MPa
μ	Viscosity	MPa·s
L	Throat length	m
η	Laryngeal tortuosity	/
v	Flow velocity	m/s
P_R	Seepage resistance	MPa
ΔP	Displacement pressure difference	MPa
P_0	Back pressure or bottom hole flowing pressure	MPa
Q	Fluid flow in throat	ml/s
a	The amount of oil replenished by the pore to the unit length of the throat	ml/s
q	The amount of oil replenished by the pore to the throat	ml/s
V_c	Effective pore volume of the core	cm^3
V_o	Oil-bearing pore volume of core	cm^3
V_t	The total volume of the throat channel in the core	cm^3
Δt	Time step	s
S	Area of throat allow seepage	m^2
$L_{\Delta t}$	Forward distance within time step Δt	m
$L_{(\Delta t, W)}$	The forward distance of water area in throat within Δt time	m
$L_{(\Delta t, O)}$	The forward distance of oil area in throat within Δt time	m
μ_w	Viscosity of water	mPa·s
μ_o	Viscosity of crude oil	mPa·s
L_w	Total length of water area in throat	m
L_o	Total length of oil area in throat	m
$\Delta P_{\Delta t}$	Actual displacement pressure difference after Δt time	MPa
L_t	Cumulative forward distance in throat within time t	m
Q_t	Output at the export end at time t	mL/s
$f(r)$	Distribution frequency of throat radius	/
n_t	Number of throats	/
n_p	Number of pores	/
r_{min}	minimum throat radius	μm
r_{max}	Maximum throat radius	μm

1. INTRODUCTION

In order to enhance the production of a single well, MLCP has become one of the most essential

technologies in the exploitation of multilayer reservoirs. However, the depositional environment may have a tremendous impact on the petrophysical characteristics of the formational rocks, notably permeability[1-3]. The MLCP seepage mechanism is complex since the physical properties of each layer vary substantially due to the high heterogeneity[4-6]. Therefore, it is difficult to describe the water-oil flow in porous media and predict the process of MLCP, both of which have a negative impact on the efficiency and effectiveness of the oil recovery plan, as well as on the recovery rate. That's why productivity dynamics of MLCP are important from both a practical and theoretical standpoint.

Well testing analysis, numerical modeling, and laboratory tests may all be utilized to forecast MLCP productivity dynamics during commingled production in general[7-14]. However, they neglected to consider the effect of continuous coupling and superposition of displacement pressure, oil viscosity, boundary layer thickness, and seepage resistance on the production efficiency of the producing well, resulting in a substantial gap between predicted and actual productivity[15]. As a result, establishing an accurate mathematical model to anticipate production performance is critical for improving MLCP recovery. There have been no attempts to develop a development performance prediction model for MLCP based on pore-throat structure and continuous iteration and coupling of the nonlinear seepage flow law.

In this study, two cores with different properties from the same well were chosen for parallel NMR on-line repulsion and contact angle experiments, and the number and distribution of pore throats at various levels in the cores were characterized using a combination of HPMI and NMR tests. The theory of seepage mechanics and the capillary tube model were used to analyze the seepage characteristics of MLCP in porous media, and the time node analysis method was used to establish a dynamic prediction model for the lifecycle process of water flooding development in heterogeneity reservoirs. This research not only offers theoretical support for projecting development behavior of the water cut and residual oil characterization in oil wells, but also helps the adjustment of development strategies in oil fields.

2. EXPERIMENTAL

2.1 Material

Two sandstone samples with permeability of 405 mD (P13-1) and 76 mD (P13-2) were found in the Ordos Basin, China (Table. 1). Two cores (P13-1 and P13-2) were cut into cylinders of the size necessary for the experiment in the procedure illustrated in Fig. 1. The oil samples were taken from formation crude oil produced in the Ordos Basin and crude oil viscosity at 60°C is 5.3 mPa·s. According to the salinity and ion concentration of formation fluids, the water utilized in the research is made up of deuterium oxide (purity: 99.99%) and inorganic salt.

Table 1. Physical properties of core sample during the NMR monitored parallel displacement experiment and the initial conditions.

Core No	Core Length/cm	Core Diameter/cm	Core Porosity/%	Permeability (nitrogen)/mD
P13-1	6.32	2.51	16.06	405
P13-2	6.02	2.51	17.19	76
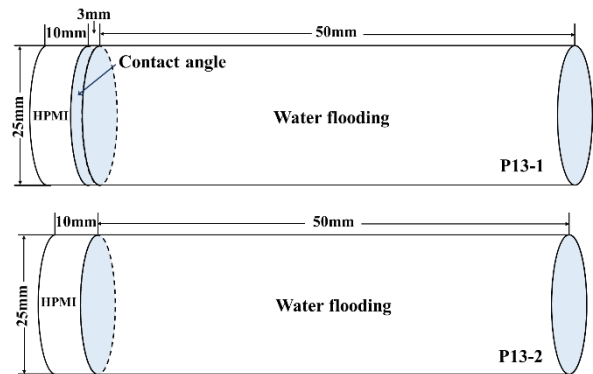
Fig. 1. The cutting position of a core sample.

2.2 Setup and Procedure

2.2.1 NMR Monitored-Displacement Apparatus

Before the NMR test, the cores were saturated with brine. Fig. 2 shows the schematic diagram, which includes a magnet, an RF emitter, and a data gathering unit. After the NMR test, the core samples were dried at 100°C for 10 hours and chilled at ambient temperature for 10 hours before being saturated by vacuum and compressed with deuterium oxide brine with a purity of 99.99 % (19 MPa).

P13-1 and P13-2 were put in separate core holders and displaced with deuterium oxide brine at the same pressure and temperature simultaneously. The cores were refilled with deuterium oxide and saturated with oil using the displacement process, with an initial displacement velocity of 0.5 ml/min, a confinement pressure of 5 MPa and an outlet pressure of atmospheric pressure, respectively. An NMR test was conducted after aging the saturated oil core for 240 hours at experimental temperature and pressure. Finally, deuterium oxide brine with a purity of 99.99 % was used to displace the cores at a constant pressure of

0.5 MPa. The water cut across the core and the oil production were measured. When the total water cut of the two samples at the outlet end reached 99.8%, the displacement was halted, and the cores were subjected to an NMR test.
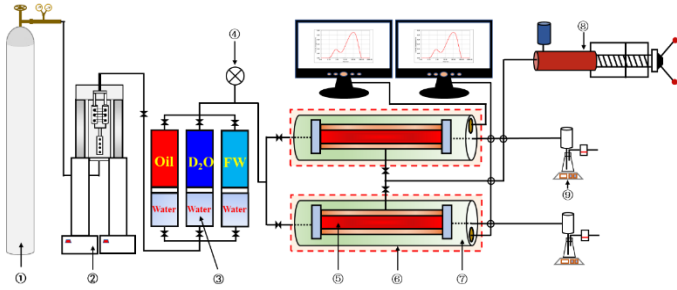
Fig. 2. Schematic of an integrated NMR and displacement system and gas permeability test device. Components: (1) High-pressure nitrogen gas bottle, (2) High-pressure syringe pump, (3) Container, (4) Pressure gauge, (5) Core holder, (6) Thermotank, (7) NMR pulsar, (8) Confining pressure pump, (9) Measuring device.

2.2.2 High Pressure Mercury Injection

The two 10 mm long cores on the left are utilized in the HPMI experiment. which were dried for 10 hours at 60°C in a continuous temperature chamber and then chilled for 10 hours at ambient temperature. For the vacuum test, the core was put in a closed high-pressure chamber, and the injection pressure was gradually increased, with the cumulative volume of mercury recorded when the pressure reached a stable level. The Washburn equation may be used to translate the mercury injection pressure to the pore-throat radius.

2.2.3 Contact Angle Measurement

The clean core was cut into slices with a diameter of 25mm and a thickness of 3mm, then polished into experimental rock slices after washing and drying. The rock slices were vacuum saturated with formation water for 12 hours in a suction filter bottle, allowing the formation water to enter the pores of the rock slices. The wetting Angle of saturated rock slices crude oil was assessed using the bubble method after they were soaked in formation water and matured for 30 days in a 75°C thermostat (Fig. 3). A CCD camera captured a real-time picture of oil droplets, and the wetting Angle was calculated.
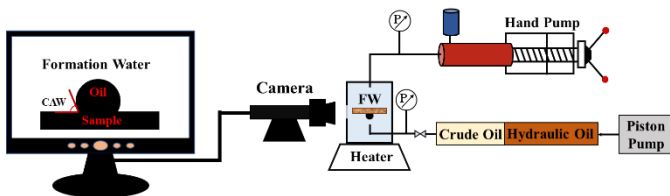
Fig. 3. Schematic of the experimental set-up for contact angle test to characterize wettability.

2.3 Experimental Result

2.3.1 NMR Monitored-Displacement Apparatus

The T_2 spectrum from saturated oil to bound water identified by NMR indicates the distribution of oil in pores and the cumulative pore volume in pores since the D_2O in the core before saturated oil does not include hydrogen atoms. The distribution of residual oil is reflected in the T_2 spectrum following displacement.

The T_2 spectrum distribution of P13-1 is shown in Fig. 4a, and the cumulative distribution of T_2 spectrum is shown in Fig. 4b. The porosity of P13-1 is 16.06 %, the porosity of oil is 13.04 %, and the porosity of residual oil is 4.84 %. The oil saturation is determined to be 82.20%, residual oil saturation is 30.14 %, and recovery is 62.88%. The results of the P13-2 NMR test are shown in Fig. 4c and Fig. 4d. The porosity of C8-2 is 17.19 %, the porosity of oil is 14.21 %, and the porosity of residual oil is 7.57 %. The oil saturation and residual oil saturation are 82.66 % and 44.04 %, respectively, and the water flooding recovery is 46.73 %, all computed using the same approach.

(a) (b)
(c) (d)
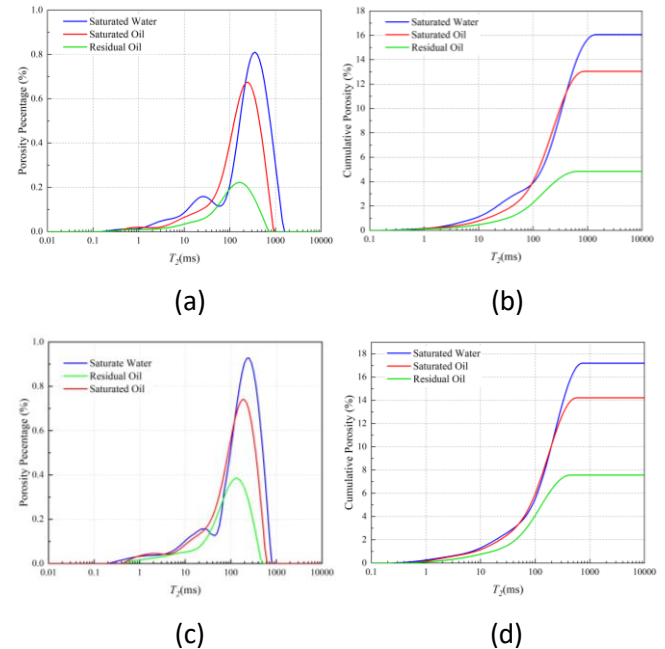
Fig. 4. NMR T_2 spectra (a) distribution and (b) cumulative of P13-1. The porosity is 16.06 %, oil saturation is 82.20%, residual oil saturation is 30.14 %, and recovery factor is 62.88%, (c) distribution and (d) cumulative of P13-2. The porosity is 17.19 %, oil saturation is 82.66 %, residual oil saturation is 44.04 %, and recovery factor is 46.73 %.

2.3.2 High Pressure Mercury Injection

In this part, HPMI was utilized to analyze the micron pores in P13-1 and P13-2. Because HPMI gathers data on the pores of the throat, as well as mercury intake and pressure, it is able to precisely portray the distribution of the throat[16]. According to Fig. 5, the capillary pressure distribution curve reveals that the throat radius size of P13-1 varied from 0.13~16.12 μm, with the principal throat radius being 10.23 μm, whereas P13-2 had a range of 0.11~8.26 μm, with a primary throat radius of 5.33 μm.
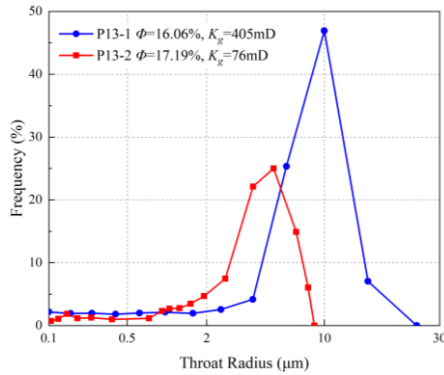
Fig. 5. Throat size and distribution frequency of P13-1 with size range 0.13 μm~16.12 μm and P13-2 with size range 0.11 μm~9.26 μm.

Table 2 Results of HPMI test.

Core NO.	Permeability/mD	Radius of Throat/μm			Number of Throat	Tortuosity
		Min	Max	Major		
P13-1	405	0.13	16.12	10.23	22102	2.58
P13-2	76	0.11	8.26	5.33	29754	

The number of P13-1 and P13-2 throats was estimated using a method that coupled NMR with HPMI (Table 2), with further details available in our earlier publications[17]. The HPMI curve represents the distribution of the throat only, and the T_2 spectrum is the response of all pores and throat signals in the core. According to the method, the pore is represented by the right peak of the T_2 spectrum, while the neck is shown by the left peak. The ratio of the peak value of the throat distribution curve formed by HPMI to the left peak of the T_2 spectrum, which is the response of all pores and throat signals in the core, while the HPMI curve indicates simply the distribution of the throat. The pore is represented by the right peak of the T_2 spectrum, meanwhile the throat is represented by the left peak, according to the procedure. Conversion coefficient (ransverse surface relaxivity rate ρ) between peak value of throat distribution curve obtained by HPMI and left peak of T_2 spectrum. The relation between relaxation time T_2 and aperture r is expressed as:

$$T_2 = \frac{1}{\rho}\frac{V}{S} = \frac{1}{\rho}\frac{r}{c} \qquad (1)$$

Fig. 6a shows the combination of throat distribution curve and T_2 spectrum of saturated water of P13-1. The T_2 value of the left peak of NMR is 25.12 ms, and the single peak of the throat distribution curve is 10.03 μm. According to Eq. (1), the ransverse surface relaxivity rate can be calculated as 0.200 μm /ms. As shown in Fig. 6b, for P13-2, The T_2 value of the left peak of NMR is 25.12 ms, the single peak of the throat distribution curve is 5.33 μm, and the ransverse surface relaxivity rate can be calculated as 0.106 μm /ms. Fig. 7 shows the pore and throat size distribution curve of P13-1 and P13-2, of which the T_2 spectrum can be converted to the pore and throat size distribution curve according to the determined ransverse surface relaxivity rate. As a consequence, the number and distribution of throats in the two cores, as well as the percentage and distribution of pore space, were determined, which served as the foundation for the modeling.

(a)   (b)
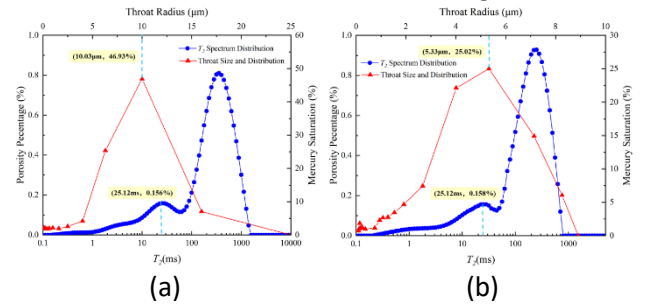
Fig. 6. Combination of throat distribution curve and T_2 spectrum of saturated water (a) P13-1, ρ=0.200 μm /ms (b) P13-2, ρ=0.106 μm /ms.

(a)   (b)
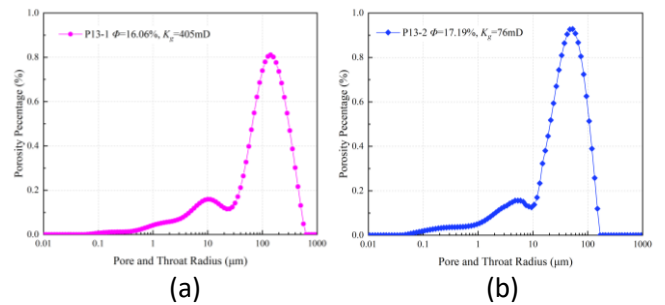
Fig. 7. Pore and throat size and distribution curve wave (a) P13-1, ρ=0.200 μm /ms (b) P13-2, ρ=0.106 μm /ms.

2.3.3 Contact Angle Measurement

Wettability is a fundamental determinant of fluid flow behavior and spatial distribution in a reservoir [18]. The contact angle of crude oil and P13-1 rock surface in the oil-formation water system is 55º in Fig. 7a, indicating that the rock surface is lipophilic according to categorization requirements. When crude oil flows in an

oil-wet reservoir, wettability hysteresis occurs, increasing the resistance to seepage. The advancing angle of crude oil on the rock surface of P13-1 is 67º, and the retreating angle is 35º, as shown in Fig. 8b, before the camera catches the oil droplet movement. P13-1 and P13-2 are samples from the same layer of the same well. In contrast to permeability, it is typically considered that wettability changes little from layer to layer and well to well, therefore the contact angles of P13-1 and P13-2 are the same in calculation.
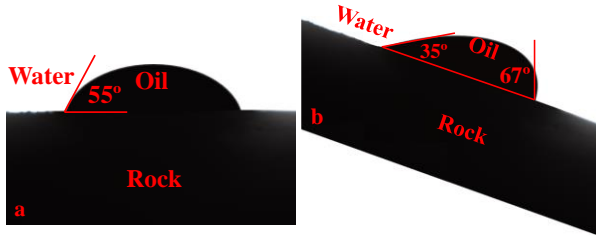
Fig. 8. Result of contact angle (a) the contact angle of the crude oil and the rock surface of P13-1 is 55º, (b) the advancing angle of crude oil on the rock surface of P13-1 is 67º and receding angle is 35º.

3. MODEL AND METHODOLOGY

3.1 Conceptual Physical Model

When water displacement takes place, the physical model of a throat in a core is shown in Fig. 9. This model assumes that there is no dissolved gas in a crude oil and that crude oil and water are not mutually soluble and diffuse. Crude oil is pumped into the throat, and no formation water is present at this point. There will be a boundary layer between water and the pore wall, which will become thinner as the displacement pressure difference increases, as the throat might be separated into water and oil zones as the process progresses. The narrower the throat, the more difficult it is for the injected water to flow. Seepage resistance is reduced because to the broad throat, high contact pressure, low interfacial tension and rapid stripping of the oil film-dominated boundary layer. In comparison to narrow pore throats, crude oil in large throats as well as the pore spaces that link them is pushed out quicker and comes into contact with water early. Due to pore throat structural inhomogeneity, water drive dynamics are more complicated for MLCP reservoir, thus the location, production capacity, and water cut of the leading edge at different positions in various throats of the cylinder were investigated using the capillary bundle model and the time-node analysis method.
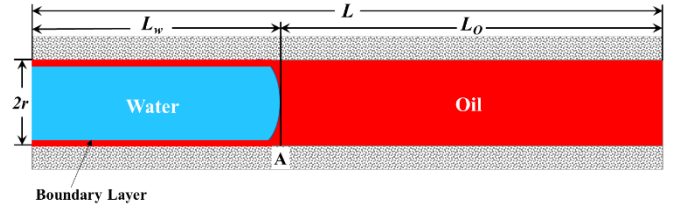
Fig. 9. Simplified physical model of water displacement with single throat, it can be divided into water area and oil area.

3.2 Model Establishment

In this section, we establish a dual-media seepage model for a single core, in which the core is divided into two media: the throat channel and the pore space, with the throat serving as the main seepage channel and the pore serving as the main oil storage space, as well as the pore space being uniformly distributed throughout the core.

3.2.1 Boundary Layer Thickness

The interaction of molecular forces on the solid-liquid interface forms the boundary layer in porous media, causing a thin coating of crude oil phase fluid to be adsorbed on the rock surface. The thickness of boundary layer of crude oil is influenced by its physical characteristics and the structure of porous media, which this model incorporates into its study of repulsion dynamics to highlight its dynamic changing features. Based on our previous research[19], we were able to derive the following equation for fitting the oil film boundary layer to the throat radius. Because the cores and crude oil used in this research are from the same region, their physical qualities are identical, as are the crude oil fractions and attributes. The equation for the thickness of the boundary layer is

$$h = (0.296 e^{\left(-5.11\frac{\Delta P}{\mu L}\right)} + 0.041)r \quad (2)$$

3.2.2 Seepage Resistance

From the contact angle test in the previous section, it is clear that the core is oil wet, so the capillary force is the resistance. Because of the interfacial tension between oil and water, which is assessed in tests that measure the contact angle, capillary force serves as a protective barrier to the entrance of injected water into the throat, the expression is

$$P_C = \frac{2\sigma \cos \theta}{r} \quad (3)$$

Wetting hysteresis at the oil-solid interface causes deformation at both ends of the curved liquid surface of

the oil droplet in the throat before it flows, necessitating the application of extra pressure to get the oil droplets to move. The second reason is that the capillary effect of oil droplets in the throat causes an extrusion pressure on the throat wall, and a big enough external pressure is required to overcome the capillary effect resistance and transfer the oil droplets. Additional resistance generated by wetting hysteresis in throats of length L may be calculated using Eq. (4)

$$P_{\mathrm{I}} = \frac{2\sigma}{r}(\cos\theta'' - \cos\theta')$$
(4)

Capillary effect resistance can be calculated using Eq. (5)

$$P_{\mathrm{II}} = \frac{2\sigma}{r}(\cos\theta - 0.5)$$
(5)

The expression formula for crude oil viscous resistance is Eq. (6)

$$P_f = \frac{2L\eta\mu v}{r^2}$$
(6)

To summarize, Eq. (7) describes the resistance of water entering the throat

$$P_R = P_C + P_I + P_{\mathrm{II}} + P_f$$
(7)

If the displacement pressure is P and the back pressure is P_0, Eq. (8) may be utilized to get the actual displacement pressure difference

$$\Delta P = P - P_R - P_0$$
(8)

3.2.2 Dynamic Prediction Model

The development behavior prediction model was built using a capillary bundle model and a temporal node analysis method. The following is a description of the oil flow via the throat

$$Q = \frac{\pi r^4}{8\mu} \cdot \frac{\Delta P}{\eta L}$$
(9)

Since the pores are uniformly distributed in the core, for a single throat of unit length, the amount of oil replenished to it by the pores is

$$a = \frac{V_o - V_t}{Ln_p}$$
(10)

Among them

$$V_o = V_c\phi$$
(11)

The total volume of the throat channel in the core is obtained from the porosity of the T_2 corresponding to the largest throat channel on the T_2 accumulation curve from the NMR test.

In time step Δt, the advancing distance of fluid in single throat is as follows

$$L_{\Delta t} = \frac{(Q - q)\Delta t}{S}$$
(12)

Where q is the amount of oil replenished by the pores to the throats

$$q = \frac{aL_{\Delta t}}{S}$$
(13)

After sorting, $L_{\Delta t}$ can be expressed as

$$L_{\Delta t} = \frac{Q\Delta t}{S + a\Delta t} = \frac{(\frac{\pi(r-h)^4}{8\mu} \cdot \frac{\Delta P}{\eta L})\Delta t}{\pi r^2 + \frac{V_o - V_t}{Ln_p}\Delta t}$$
(14)

Given that the fluid migration distance between the two locations is equal at any given moment, the following function can be established

$$L_{\Delta t} = L_{(\Delta t, W)} = L_{(\Delta t, O)} = \frac{(\frac{\pi(r-h)^4}{8\mu_w} \cdot \frac{\Delta P_w}{\eta L_w})\Delta t}{\pi r^2 + \frac{V_o - V_t}{Ln_p}\Delta t} = \frac{(\frac{\pi(r-h)^4}{8\mu_o} \cdot \frac{\Delta P_o}{\eta L_o})\Delta t}{\pi r^2 + \frac{V_o - V_t}{Ln_p}\Delta t}$$
(15)

After the displacement time Δt, the range of two areas changed, thus the displacement resistance, displacement front pressure, boundary layer thickness, and other parameters changed as well, resulting in the real displacement pressure difference of

$$\Delta P_{\Delta t} = P - P_0 - \frac{2\sigma_{(\Delta P_i, W-O)}}{r}(2\cos\theta + \cos\theta'' - \cos\theta' - 0.5) - \frac{2(L_o - L_{\Delta t})\eta v_{\Delta t}\mu_o}{r^2}$$
(16)

The cumulative migration distance of fluid in the throat is calculated as follows when displacement time is t

$$L_t = \int_0^t L_{\Delta t}dt$$
(17)

At time t, production at the export end is represented as

$$Q_t = \int_{r_{\min}}^{r_{\max}} n_t f(r)Q_o dr$$
(18)

The initial conditions as follows

$$\begin{cases} L = L_o \\ P_f = 0 \end{cases}$$
(19)

Eq. (16)~(19) constitute the development performance prediction model of water flooding for lifecycle process in MLCP reservoir. It can be used to calculate production, water cut and cumulative production at any time during water flooding.

4. VALIDATION AND APPLICATION

4.1 Calculation Process

A smaller time step enhances model accuracy, but it comes at the cost of longer calculation and operation times. The choice of the t value is crucial to solving the

model. An acceptable time constant t value may be calculated based on real-world computer performance and computation accuracy requirements. To calculate Eqs. (16) ~ (19) and anticipate production, water cut and cumulative production at different time-instances, the Newton-Raphson iterative numerical solution approach may be utilized. A 1 second time step is used. The calculation process is implemented in Python programming and the whole flowchart is shown in Fig. 10.
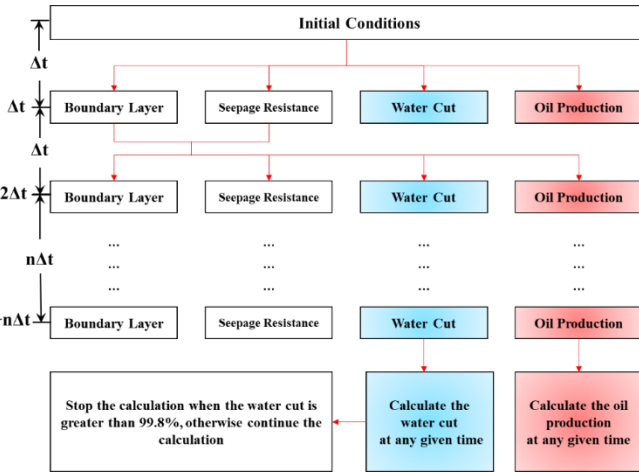
Fig. 10. Flow chart for calculation of development performance prediction model for water flooding lifecycle.

4.2 Model Validation

Fig. 11 illustrates the link between recovery ratio and water parallel displacement time for P13-1 and P13-2. Because the permeability is lower and the seepage resistance is greater in P13-2 than in P13-1, water-oil travels more slowly in the throat. The seepage resistance reduces as the displacement improves, and the slope of the recovery curve increases. The calculation matched the experimental recovery curve well. As shown in Fig. 11a, at the end of the 500th minute, the experimental recovery and the calculated recovery of P13-1 is 62.88 % and 65.96 %, respectively, with an uncertainty is 4.89 %. The water cut of experimental and calculated of P13-1 is 99.8 % and 99.54 %, respectively, with a 0.26 % uncertainty. Fig. 11b shows the experimental and calculated recovery of P13-2 is 46.73 % and 45.33 %, respectively, with an uncertainty of 2.99 %, while the water cut of experimental and calculated is 36.45% and 35.37%, respectively, with an uncertainty of 2.99 %. Overall, the experimental findings matched those of the calculations, demonstrating that the model is accurate.

(a)   (b)
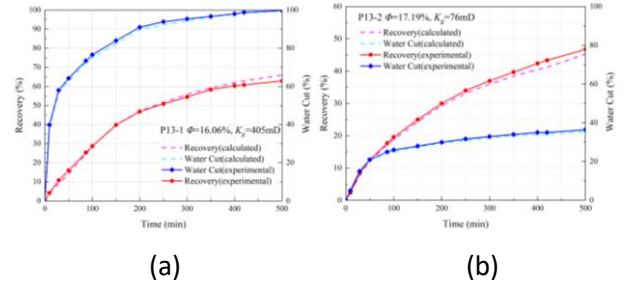
Fig. 11. Graph depicting the development performance of water floods throughout the course of a lifecycle process, as determined by both experimental and model methods. In comparison to the experimental findings, recovery error and water cut error value of P13-1 is 4.89 % and 0.26 %, respectively; recovery error and water cut error value of P13-2 both 2.98 %.

After a water parallel displacement experiment, the predicted oil saturation distribution in the core is shown in Fig. 12. The oil saturation rises progressively from left to right along the displacement path, indicating that P13-1 was entirely displaced near the intake. The oil saturation ranges from 33.21 % to 46.72 % in the oil region front to the outlet, with an average residual oil saturation of 30.14 %. The P13-2 has a far higher residual oil saturation than the P13-1, after the displacement was completed, the residual oil saturation at the outlet was 65.56 %, and the average residual oil saturation was 44.04 %.
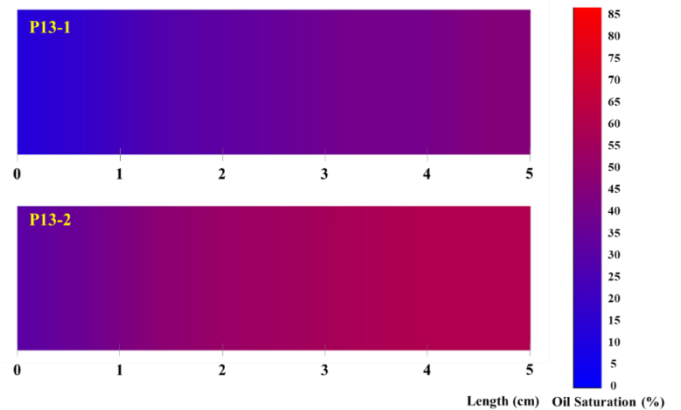
Fig. 12. Plane diagram of residual oil distribution after water parallel flooding. The average remaining oil saturation of P13-1 and P13-2 is 30.14 % and 44.04 %, respectively (The initial oil saturation of P13-1 and P13-2 is 82.20% and 82.66 %, respectively).

5. CONCLUSION

NMR, HPMI, and contact angle testing were used in a MLCP water drive process to study the influence of pore throats at different levels in the core on the recovery rate. The time node analysis method was used to establish a dynamic prediction model for the lifecycle

process of water flooding development in multilayer heterogeneity reservoirs, and the theory of seepage mechanics and the capillary tube model were used to analyze the seepage characteristics of MLCP in porous media. Differences in boundary layer thickness, water cut, recovery degree, and seepage resistance in various radius throats are continually iterated and connected to one other, resulting in early water breakthrough and

displacement in big throats than in small throats. The deviations of model are within the acceptable range, suggesting that it is trustworthy. This study offers a valuable technological technique for optimizing development strategy and adjusting development plans in real-world settings.

REFERENCE

[1] Abdlmutalib AJ, Ayranci K, Yassin MA, Hussaini SR, Abdullatif OA, Humphrey JD. Impact of sedimentary fabrics on small-scale permeability variations within fine-grained sediments: Early Silurian Qusaiba Member, Northern Saudi Arabia. Marine and Petroleum Geology. 2022;139.

[2] Akrout D, Cobbold PR, Ahmadi R, Mercier E, Montacer M. Physical modelling of sub-salt gliding due to fluid overpressure in underlying sedimentary strata. Marine and Petroleum Geology. 2016;72:139-55.

[3] Yancheng L, Xianbo L, Kai K, Tingli L, JIANG S, ZHANG J, et al. Permeability characterization and directional wells initial productivity prediction in the continental multilayer sandstone reservoirs: A case from Penglai 19-3 oil field, Bohai Bay Basin. Petroleum Exploration and Development. 2017;44:97-104.

[4] Chai X, Tian L, Dong P, Wang C, Peng L, Wang H. Study on recovery factor and interlayer interference mechanism of multilayer co-production in tight gas reservoir with high heterogeneity and multi-pressure systems. Journal of Petroleum Science and Engineering. 2022;210.

[5] Peng S, Jia L, Xu J, Zhang C, Li Q, Han E. The production schedule optimization of a multilayer superposed CBM system: An experimental study. Powder Technology. 2020;373:99-108.

[6] Wang L, Yang S, Liu Y, Xu W, Deng H, Meng Z, et al. Experiments on gas supply capability of commingled production in a fracture-cavity carbonate gas reservoir. Petroleum Exploration and Development. 2017;44:824-33.

[7] Buckley SE, Leverett M. Mechanism of fluid displacement in sands. Transactions of the AIME. 1942;146:107-16.

[8] Dykstra H, Parsons R. The prediction of oil recovery by water flood. Secondary recovery of oil in the United States. 1950;2:160-74.

[9] Lefkovits H, Hazebroek P, Allen E, Matthews C. A study of the behavior of bounded reservoirs composed of stratified layers. Society of Petroleum Engineers Journal. 1961;1:43-58.

[10] Bourdet D. Pressure behavior of layered reservoirs with crossflow. SPE California regional meeting: OnePetro; 1985.

[11] Tompang R, Kelkar B. Prediction of waterflood performance in stratified reservoirs. Permian Basin Oil and Gas Recovery Conference: OnePetro; 1988.

[12] El-Khatib NA. The application of Buckley-Leverett displacement to waterflooding in non-communicating stratified reservoirs. SPE Middle East Oil Show: OnePetro; 2001.

[13] Huang S, Kang B, Cheng L, Zhou W, Chang S. Quantitative characterization of interlayer interference and productivity prediction of directional wells in the multilayer commingled production of ordinary offshore heavy oil reservoirs. Petroleum Exploration and Development. 2015;42:533-40.

[14] El-Khatib NA. The modification of the dykstra-parsons method for inclined stratified reservoirs. SPE Journal. 2012;17:1029-40.

[15] Wang H, Tian L, Chai X, Wang J, Zhang K. Effect of pore structure on recovery of CO_2 miscible flooding efficiency in low permeability reservoirs. Journal of Petroleum Science and Engineering. 2022;208:109305.

[16] Jiang L-L, Tian L, Zhou Y-T, Li M, Huang C, Wang J-X, et al. Prediction of Minimum Miscibility Pressure for CO_2 Flooding Based on Microscopic Pore-Throat Structure. Frontiers in Energy Research. 2022;10.

[17] Tian L, Wang H, Wu T, Yang H, Xu S, Chai X, et al. In-depth analysis of ultrasonic-induced geological pore re-structures. Ultrasonics sonochemistry. 2022;85:1059-90.

[18] Anderson WG. Wettability literature survey-part 1: rock/oil/brine interactions and the effects of core handling on wettability. Journal of petroleum technology. 1986;38:1125-44.

[19] Wang H, Tian L, Gu D, Li M, Chai X, Yang Y. Method for calculating non-darcy flow permeability in tight oil reservoir. Transport in Porous Media. 2020;133:357-72.